PPPL-2050

Dr. 1966-6

MODE CONVERSION AND ELECTRON HEATING NEAR THE UPPER HYBRID RESONANCE FREQUENCY

PPPL--2050

DE84 003465

By

B.L. Smith, H. Okuda, and H. Abe

NOVEMBER 1983

PLASMA PHYSICS LABORATORY

PRINCETON UNIVERSITY

PRINCETON, NEW JERSEY

PREPARED FOR THE U.S. DEPARTMENT OF ENERGY,
UNDER CONTRACT DE-AC02-76-CHO-3073.

DISCLAIMER

MODE CONVERSION AND ELECTRON HEATING NEAR THE UPPER HYBRID RESONANCE FREQUENCY

Bruce L. Smith and H. Okuda

Plasma Physics Laboratory, Princeton University

Princeton, New Jersey 08544

and

H. Abe

Department of Electronics, Kyoto University

Kyoto 606, Japan

ABSTRACT

Mode conversion near the upper hybrid resonance frequency and electron heating are studied using a one-dimensional electromagnetic relativistic particle code. It is found that for a sufficiently small pump field E_o, $E_o^2/4\pi nT_e \lesssim 0.01$, electron heating is localized in a region near the electron cyclotron layer where the pump frequency is equal to the local electron gyrofrequency. For stronger pump fields, electron heating takes place more or less uniformly across a region between the upper hybrid resonance layer and the cyclotron layer. In addition, a significant fraction of electromagnetic energy associated with the pump is found to be reflected back into the vacuum from a region in the plasma near the upper hybrid resonance layer for both strong $(E_o^2/4\pi nT_e \approx 1)$ and weak pumps $(E_o^2/4\pi nT_e \ll 1)$.

I. INTRODUCTION

Mode conversion at the upper hybrid layer has been studied extensively by means of linear theory,[1-3] nonlinear theory[4] and with computer simulations.[5] It has been pointed out that an extraordinary wave normally incident along a decreasing magnetic field mode converts into a short wavelength electrostatic wave at the upper hybrid layer. The mode-converted electrostatic wave propagates back toward the high magnetic field side until it is absorbed at the electron cyclotron layer where the wave frequency is equal to the electron gyrofrequency. At the upper hybrid layer where a short wavelength, large amplitude electrostatic wave is generated, however, a linear theory may not adequately describe the process, and nonlinear effects must be taken into account in order to estimate the limiting amplitude and the efficiency of energy conversion to electrostatic waves.

We have studied wave propagation and electron heating in some detail using a one-dimensional electromagnetic relativistic particle simulation model. We find in the simulation that an extraordinary wave launched from the high magnetic field side suffers little attenuation at the cyclotron layer before reaching the upper hybrid layer where the mode conversion takes place. The mode-converted electrostatic wave propagates backwards, causing substantial heating of electrons. When the pump amplitude is sufficiently small, $E_o^2/4\pi nT_e \lesssim 0.01$, electron heating is localized near the cyclotron layer. For stronger pump amplitudes, substantial electron heating takes place more or less uniformly across a region between the upper hybrid layer and the cyclotron layer. In addition, a significant amount of electromagnetic energy is found to be reflected back from the plasma near the upper hybrid layer. The reflected electromagnetic waves eventually leave from the plasma back into the vacuum region.

II. SIMULATION RESULTS

The one-dimensional electromagnetic, relativistic particle code used in the simulation is similar to that of Lin[5] where a slab of electrons with uniform density, $n(x)$, is embedded in an inhomogeneous dc vacuum magnetic field, $B_o(x)\hat{z}$. Ions are immobile in this model, eliminating certain classes of nonlinear processes associated with the mode conversion. The magnetic field decreases linearly with distance, and the nonrelativistic electron gyrofrequency is $\omega_c = 2.5$ at the left boundary of the plasma and $\omega_c = 1.5$ at the right boundary in units used in the simulations. The plasma density is uniform across the slab, and the electron plasma frequency is $\omega_{pe} = \sqrt{2}$.

The total simulation length is 1024 grids, $L = 1024\Delta$, where the initial electron Debye length is $1/\sqrt{2}\Delta$. The plasma slab is located at between $x = 256\Delta$ and $x = 768\Delta$, and the antenna is at $x = 216\Delta$. The antenna is located in the vacuum region at the high magnetic field side at a distance from the plasma a little greater than one half of a pump wavelength. Such a distance is necessary for the measurement of radiation coming from the plasma slab. The antenna consists of a sheet current, $J_y \exp(i\omega_o t)$, oscillating at the pump frequency $\omega_o = 2.25$ located at a computational mesh point. Absorbing boundary conditions are imposed on the electromagnetic fields at both the left and right boundaries and are achieved by the use of lamp functions.[6] The speed of light is taken $c = 20\Delta\ \bar{\omega}_{pe}$, where $\bar{\omega}_{pe}$ is the average plasma frequency including the vacuum region and is taken to be unity in the code. From these numbers, one finds that the cyclotron layer ($\omega_c = \omega_o$) is located at $x = 384\Delta$, and the cold plasma upper hybrid resonance layer ($\omega_o^2 = \omega_{pe}^2 + \omega_c^2$) at $x = 640\Delta$. The model is depicted in Fig. 1.

The initial ratio of the electron thermal speed, v_t, to the speed of light is taken $v_t/c = 0.05$, corresponding to a plasma temperature slightly

higher than 1 keV. The strength of the pump may be given by the ratio of the oscillating speed $v_o = e E_o/m\omega_o$ to the thermal speed of electrons, and four different pump strengths are considered here. The first (Case 1) is $v_o/v_t = 0.88$, the second (Case 2) is $v_o/v_t = 0.44$, the third (Case 3) is $v_o/v_t = 0.176$, and the fourth (Case 4) is $v_o/v_t = 0.088$. The pump strength can alternatively be given by the ratio of the pump wave energy density to the electron thermal energy density, $E_o^2/4\pi nT_e$. In terms of this parameter, the four cases correspond to $E_o^2/4\pi nT_e = 0.98$, 0.245, 0.039, and 0.0098, respectively. We shall describe the strong pump case first followed by the weaker pump cases.

A. Case 1: $v_o/c = 0.044$, $v_o/v_t = 0.88$, $E_o^2/4\pi nT_e = 0.98$

Let us first study a strong pump case. Figure 2 shows the instantaneous profile of the electrostatic, E_x, and electromagnetic, E_y, fields before, $t = 140\ \bar{\omega}_{pe}^{-1}$, and after the mode conversion, $t = 400\ \bar{\omega}_{pe}^{-1}$. Here all the fields are normalized to the dc magnetic field at the center of the plasma column, $x = 512\Delta$. Note at the speed of light $c = 20\Delta\bar{\omega}_{pe}$ the electromagnetic wave would have propagated as much as 2800Δ by $t = 140\ \bar{\omega}_{pe}^{-1}$, much farther than the system size, $L = 1024\Delta$, if no plasma existed. Instead, both the group and phase velocities of the pump wave become smaller as the wave front approaches the upper hybrid resonance layer. The induced electrostatic field associated with the upper hybrid pump wave becomes larger in time as more and more electromagnetic energy is converted into the electrostatic wave. Near the resonance layer, the wavelength of the electric fields is slightly shorter than the free space wavelength. Mode conversion to short wavelength electrostatic waves has not taken place at $t = 140\bar{\omega}_{pe}^{-1}$, shown in the top panel, while at $t = 400\bar{\omega}_{pe}^{-1}$, shown in the bottom panel, the mode-converted

waves have reached the cyclotron layers.

The mode-converted electrostatic wave propagates toward the high magnetic field side with a group velocity on the order of the electron thermal speed until it reaches the cyclotron layer where strong absorption takes place. The instantaneous plots of E_x and E_y at $t = 400\bar{\omega}_{pe}^{-1}$, where the converted electrostatic waves reached the cyclotron layer, are shown in the bottom panel of Fig. 2. Note that E_y is no longer as coherent as it was in the top panel of Fig. 2 for the incoming pump wave. Spectrum analysis reveals that, at this time, a significant amount of incident wave energy is reflected back to the high magnetic field side. The electrostatic field, E_x, becomes essentially turbulent, with many modes at different wavelengths excited and propagating in both directions.

Figure 3 shows the corresponding phase space plots of the electrons at $t = 140\bar{\omega}_{pe}^{-1}$, top panel, and $t = 400\bar{\omega}_{pe}^{-1}$ at the bottom panel. Here v_x and v_y represent the x- and y- components of the momentum p_x, p_y, divided by the non-relativistic mass m_o. At $t = 140\bar{\omega}_{pe}^{-1}$, both v_x and v_y show distinct modulation by the large amplitude wave, $v_o/v_t = 0.88$. In addition, a clear sign of the acceleration in $v_x - v_y$ space is seen near the cyclotron layer at $x = 384\Delta$. This is evidence for the electron cyclotron resonance at the cyclotron layer associated with the right-hand component of the pump wave. While the right-hand component vanishes at the cyclotron layer in a cold plasma theory, inclusion of finite-gyro radius effects leads to a small but nonzero component.

Heating of electrons at $t = 400\bar{\omega}_{pe}^{-1}$ after the mode conversion is shown in the bottom panel of Fig. 3. Note the coherent structure of the modulations seen at earlier times is gradually thermalized for both v_x and v_y. It is clear that significant electron heating can take place more or less uniformly

across a broad region between the upper hybrid layer and the cyclotron layer with a strong pump. Note large acceleration near the cyclotron layer, $\omega_o = \omega_{ce}$, generates a group of energetic electrons associated with the cyclotron damping.

It is important to study the amount of wave energy absorbed in a plasma and reflected back into vacuum in order to estimate the efficiency of heating. Let us first decompose the waves into the left- and right-going components. This can be done first by filtering the field at each grid point with the pump frequency ω_o,

$$E_y(\omega_o,x) = \frac{1}{t_2-t_1}\int_{t_1}^{t_2} E_y(t,x)\, e^{i\omega_o t}dt \ , \tag{1}$$

and then Fourier analyzing $E_y(\omega_o, x)$ in k-space,

$$E_y(\omega_o,k) = \frac{1}{L}\int_o^L E_y(\omega_o,x)e^{-ikx}dx \quad . \tag{2}$$

The distribution of E_y with respect to k provides information about the amplitude of reflected and transmitted waves. This analysis may be carried out over the entire plasma column or locally. Similar diagnostics can be carried out for the electrostatic field. Frequency analysis indicates that essentially all the wave energy is at the pump frequency $\omega = \omega_o$, and very little is left for the harmonics.

Figure 4 shows the k-spectrum obtained by integrating Eq. (2) over the entire plasma slab for both longitudinal, $E_x(\omega_o,k)$, left column, and transverse, $E_y(\omega_o,k)$, right column, fields at different times. The pump wave, $E_y(\omega_o,k)$, has two distinct peaks at the mode numbers slightly higher than the free space wavenumbers $k_o = \pm\omega_o/c$ corresponding to $m \simeq \pm$ 18. In addition, a

sharp peak near $k \approx 0$ is seen for both E_x and E_y corresponding to the average field of the system, which does not vanish for non-periodic boundary conditions. At earlier times, $t = 200\,\bar{\omega}_{pe}^{-1}$, shown by the top panel, most of the wave energy is at $k \approx \omega_o/c$ corresponding to the pump wave propagating into a plasma slab. The smaller peak at $k \approx -\omega_o/c$ for E_y corresponds to the wave propagating to the left from the antenna, and such left-going waves are absorbed at the boundaries.

At time $t = 400\bar{\omega}_{pe}^{-1}$ given by the middle panel when the mode-converted waves reached the cyclotron layer as shown in Fig. 3, a significant number of reflected electromagnetic waves are seen and become larger than the incoming waves at time $t = 600\bar{\omega}_{pe}^{-1}$, shown in the bottom panel. It is clear that the conversion to electrostatic short wavelength waves from long wavelength electromagnetic waves is not 100%.

E_x, the electrostatic field, shown in the left column of Fig. 4, behaves quite differently from its electromagnetic counterpart. At an early time, $t = 200\bar{\omega}_{pe}^{-1}$, shown at the top panel, the spectrum has a well-defined peak near k corresponding to the extraordinary pump wave. As the mode conversion process takes place, the spectrum spreads to both short and long wavelengths in both directions of propagation so that it becomes quite broad as seen in the middle and bottom panels, showing a sign of strong plasma turbulence.

In order to study the reflected wave energy quantitatively, the time averaged Poynting energy flux, $P_x = cE_yB_z/4\pi$, is measured at a vacuum region between the antenna and the plasma at different times. This was done by first decomposing E_y and B_z into left and right propagating components and then calculating the flux. The results are shown in Fig. 5. Poynting flux is normalized to the flux at the antenna. Solid circles correspond to the right going waves and open circles are for left going waves. It is interesting to

observe that little reflection takes place until $t \approx 450\bar{\omega}_{pe}^{-1}$ when a significant amount of energy is radiated back to the vacuum region. Local diagnostics for the Poynting flux confirm that the incident extraordinary wave is partially mode converted to electrostatic waves and partially reflected near the upper hybrid layer. This is discussed in the next case.

B. Case 2: $v_o/c = 0.022$, $v_o/v_t = 0.44$, $E_o^2/4\pi nT_e = 0.25$

When the pump amplitude is reduced, plasma heating and the propagation speed of the reflected wave towards the high magnetic field side become slower. The general physical picture of mode conversion and wave reflection, however, remains the same. Using the same simulation parameters as in Case 1 except that the pump strength is reduced by a factor of 2, the second simulation is carried out.

Figure 6 shows the instantaneous fields E_x and E_y at $t = 400\bar{\omega}_{pe}^{-1}$. Comparing Fig. 6 with Fig. 2, we note that the mode-converted wave has not reached the cyclotron layer yet in this example (while it took only $t \approx 300\bar{\omega}_{pe}^{-1}$ for Case 1). The reason for this is that the group velocity of the electrostatic Bernstein wave is on the order of the electron thermal speed so that the propagation velocity of the electrostatic waves becomes smaller as the heating associated with the mode conversion becomes smaller. The incoherent nature of E_y shown in Fig. 6(b) indicates the presence of a significant amount of reflection near the resonance layer.

Strong electron heating takes place between the resonance and cyclotron layers at $t = 1500\bar{\omega}_{pe}^{-1}$, as shown in Fig. 7, where bulk heating as well as a high energy tail are clearly observed. This heating is similar to that of Case 1, and both cases demonstrate that heating can take place more or less uniformly between the resonance layer and the cyclotron layer.

The strong turbulent nature of the longitudinal field, E_x, and large amounts of reflection can again be seen as shown in Fig. 8. Comparing Fig. 8 with Fig. 4, we note the qualitative features of both cases are similar with respect to wave reflection. The primary difference is that it takes a longer time to generate the reflection for a weaker pump. The measurements of the Poynting flux at the vacuum region between the antenna and the plasma boundary shown in Fig. 9 indicate reflection of significant amounts of electromagnetic energy back into the vacuum region at $t \approx 800\bar{\omega}_{pe}^{-1}$, in agreement with the spectrum analysis of Fig. 8.

In order to locate the reflection point of the electromagnetic waves in more detail, local Poynting flux is time-space Fourier analyzed, as shown in Fig. 10. This is done by first dividing the total system length $L = 1024\Delta$ into eight segments, each having 128Δ width. At each segment, the Poynting flux, $cE_yB_z/4\pi$, is Fourier decomposed into left- and right-going waves at $\omega = \omega_o$. Three segments centered at $x = 320\Delta$ (left column), $x = 448\Delta$ (middle column), and $x = 576\Delta$ (right column) are shown at $t = 240\bar{\omega}_{pe}^{-1}$ (top panel) and $t = 464\bar{\omega}_{pe}^{-1}$ (bottom panel). Let us first study the bottom panel, $t = 464\bar{\omega}_{pe}^{-1}$. At three locations shown in (d), (e), (f), both left- and right-going waves are observed. The sharp peak near $m = -4$ corresponds to the free space wavelength of the pump frequency, $k = -\omega_o/c$. At $x = 320\Delta$, the Poynting flux going to the left is larger than that going to the right, while the fluxes are comparable at $x = 448\Delta$. At $x = 576\Delta$, the dominant peak has long wavelength, $k \ll \omega_o/c$, while the reflected waves are larger than the right-going waves. Beyond the resonance layer, very little energy is found. In contrast the top panel at $t = 240\bar{\omega}_{pe}^{-1}$ shows that while a reflected component may exist even at this early time the transmitted wave clearly is dominant [panel (c)]. It is clear from these observations that both left- and right-

going electromagnetic waves exist simultaneously between the pump antenna and the resonance layer.

C. Case 3: $v_o/c = 0.0088$, $v_o/v_t = 0.176$, $E_o^2/4\pi nT_e = 0.038$

With the further reduction of pump amplitude, the propagation speed of the mode-converted waves becomes still slower, confirming that the propagation speed is of the order of the electron thermal speed. Figure 11 shows the instantaneous temperature profiles, T_x, T_y, at $t = 1000\bar{\omega}_{pe}^{-1}$, (a), (b), and $2000\bar{\omega}_{pe}^{-1}$, (c), (d), where the temperature is defined as the average kinetic energy normalized by the initial kinetic energy. The reflected waves are observed to have reached the cyclotron layer at $t = 1000\bar{\omega}_{pe}^{-1}$. Again the heating takes place at a region between the resonance and cyclotron layer and is not localized at the cyclotron layer as is shown for the stronger pump.

As in the other two cases, reflection of the electromagnetic wave is seen again shown in Fig. 12. The amplitude of the reflected wave near the resonance layer becomes about the same as the incident wave's by $t = 1600\bar{\omega}_{pe}^{-1}$. The electrostatic field again shows a complex spectrum. Long and short wavelengths are seen clearly indicating the presence of mode converted short waves as well as extraordinary waves, both propagating in the two directions. Figure 13 shows the Poynting flux measured at the vacuum with a significant reflection as before.

D. Case 4: $v_o/c = 0.0044$, $v_o/v_t = 0.088$, $E_o^2/4\pi nT_e = 0.0098$

The last example considered is for the smallest pump amplitude, $E_o^2/4\pi nT_e = 0.0098$, which is comparable with laboratory experiments. First we shall study the heating of electrons as shown in Fig. 14. The measured temperature profiles, $T_x(x)$ and $T_y(x)$, are shown at $t = 900\bar{\omega}_{pe}^{-1}$, top panel

(a), (b), and $1600\bar{\omega}_{pe}^{-1}$, bottom panel, (c), (d), in this case. At $t = 900\bar{\omega}_{pe}^{-1}$, both T_x and T_y have sharp peaks near the cyclotron layer, $\omega_o = \omega_{ce}$, as predicted by linear theory. The temperature gradient near the cyclotron layer is extremely large since electrons cannot leave this layer in our one-dimensional model. If, on the other hand, electrons are allowed to stream out from the cyclotron layer along the magnetic field, the resultant temperature gradient would remain small. At a later time, $t = 1600\bar{\omega}_{pe}^{-1}$, shown in the bottom panel, the heated region expanded although it is still well confined near the cyclotron layer. This is in sharp contrast to the stronger pump case where the heating layer was more or less uniformly spread between the resonance and cyclotron layers as shown in Figs. 3, 7, and 11.

Wave reflection does take place even for such a weak pump as shown in Fig. 15 where the time averaged Poynting flux is plotted at four different times, $t = 12.5$, 137.5, 412, and $1235\bar{\omega}_{pe}^{-1}$. The antenna is located at $x = 216\Delta$ where a jump of the flux to the left (negative) and to the right (positive) directions exists. At early times, (a) and (b), the amplitude of the flux near the antenna is about the same for waves propagating left and right, while at later times, (c) and (d), the Poynting flux to the right begins to diminish to a much smaller level compared to the left-going component. The mechanism for reflection is not completely understood at present, although several processes, such as nonlinear effects due to the large electrostatic field near the resonance layer or the inverse mode-conversion process which converts electromagnetic radiation from the short wavelength electrostatic waves generated by hot electrons,[7] may be possible. The sharp temperature gradient near the cyclotron layer does not seem important since the reflection takes place beyond the cyclotron layer.

III. CONCLUSIONS

A one-dimensional electromagnetic simulation model is used to study electron heating and wave reflection associated with the upper hybrid resonance for different pump strengths. A significant amount of electromagnetic energy is reflected back to the vacuum region from plasma near the resonance layer.

The fraction of reflection is rather insensitive to the pump amplitude. For a weak pump amplitude, $E_o^2/4\pi nT_e \lesssim 0.01$, electron heating is localized near the cyclotron layer. Significant electron heating takes place more or less uniformly in a region between the upper-hybrid resonance and cyclotron layer for larger pump amplitudes. Whether or not the results found in this paper need modification in two-dimensions remains to be seen. In particular the role of finite parallel wavelengths and the parallel electron motion are not considered in this calculation ($k_{\parallel} = 0$). Furthermore, reflection and wave propagation in two-dimensions are certainly very important. These subjects will be considered in the future.

ACKNOWLEDGMENTS

The authors would like to thank Dr. V. Arunasalam, Dr. H. Hsuan, and Dr. A. T. Lin for their encouragement and stimulating discussions.

This work was supported by the United States Department of Energy Contract No. DE-AC02-76-CHO-3073 and the National Science Foundation Contract ATM-83-1102.

One of the authors (BLS) acknowledges the support of the Fannie and John Hertz Foundation.

REFERENCES

1. T. H. Stix, Phys. Rev. Lett. 15, 878 (1965).

2. R. B. White and F F. Chen, Plasma Phys. 16, 565 (1974).

3. J. J. Schuss and J. C. Hosea, Phys. Fluids 18, 727 (1975).

4. Merit Shoucri and H. K. Kuehl, Phys. Fluids 23, 2461 (1980).

5. A. T. Lin and C. C. Lin, Phys. Rev. Lett. 47, 98 (1981).

A. T. Lin, C. C. Lin, and J. M. Dawson, Phys. Fluids 25, 646 (1982).

6. P. C. Liewer, A. T. Lin, J. M. Dawson, and M. Z. Caponi, Phys. Fluids 24, 1364 (1981).

7. J. Hosea, V. Arunasalam, and R. Cano, Phys. Rev. Lett. 39, 408 (1977).

FIGURE CAPTIONS

FIG. 1. One-Dimensional Model.

FIG. 2. Instantaneous profiles of the electrostatic, E_x, and electromagnetic, E_y, fields at $t = 140\bar{\omega}_{pe}^{-1}$ (top) and $400\bar{\omega}_{pe}^{-1}$ (bottom). Case 1.

FIG. 3. Electron phase space plots at $t = 140\bar{\omega}_{pe}^{-1}$ (top) and $400\bar{\omega}_{pe}^{-1}$ (bottom). Case 1.

FIG. 4. Spectrum analysis for the electrostatic (left) and electromagnetic (right) fields at three different times. Case 1.

FIG. 5. Poynting flux measured at the left boundary of the plasma slab. Case 1.

FIG. 6. Instantaneous profiles of the electrostatic, E_x, and electromagnetic, E_y, fields at $t = 400\bar{\omega}_{pe}^{-1}$. Case 2.

FIG. 7. Electron phase space and the particle distribution at $t = 1500\bar{\omega}_{pe}^{-1}$. Case 2.

FIG. 8. Spectrum analysis for the electrostatic (left) and electromagnetic (right) fields at four different times. Case 2.

FIG. 9. Poynting flux measured at the left boundary of the plasma slab. Case 2.

FIG. 10. Spectrum analysis for the Poynting flux at t = $240\bar{\omega}_{pe}^{-1}$(top) and $464\bar{\omega}_{pe}^{-1}$(bottom) at three different locations. Case 2.

FIG. 11. Electron temperature profile at t = $1000\bar{\omega}_{pe}^{-1}$ (top) and $2000\bar{\omega}_{pe}^{-1}$ (bottom). Case 3.

FIG. 12. Spectrum analysis for the electrostatic (left) and electromagnetic (bottom) fields at three different times. Case 3.

FIG. 13. Poynting flux measured at the left boundary of the plasma slab. Case 3.

FIG. 14. Electron temperature profile at t = $900\bar{\omega}_{pe}^{-1}$ (top) and $1600\bar{\omega}_{pe}^{-1}$ (bottom). Case 4.

FIG. 15. Time-averaged Poynting flux measured locally at four different times. Case 4.

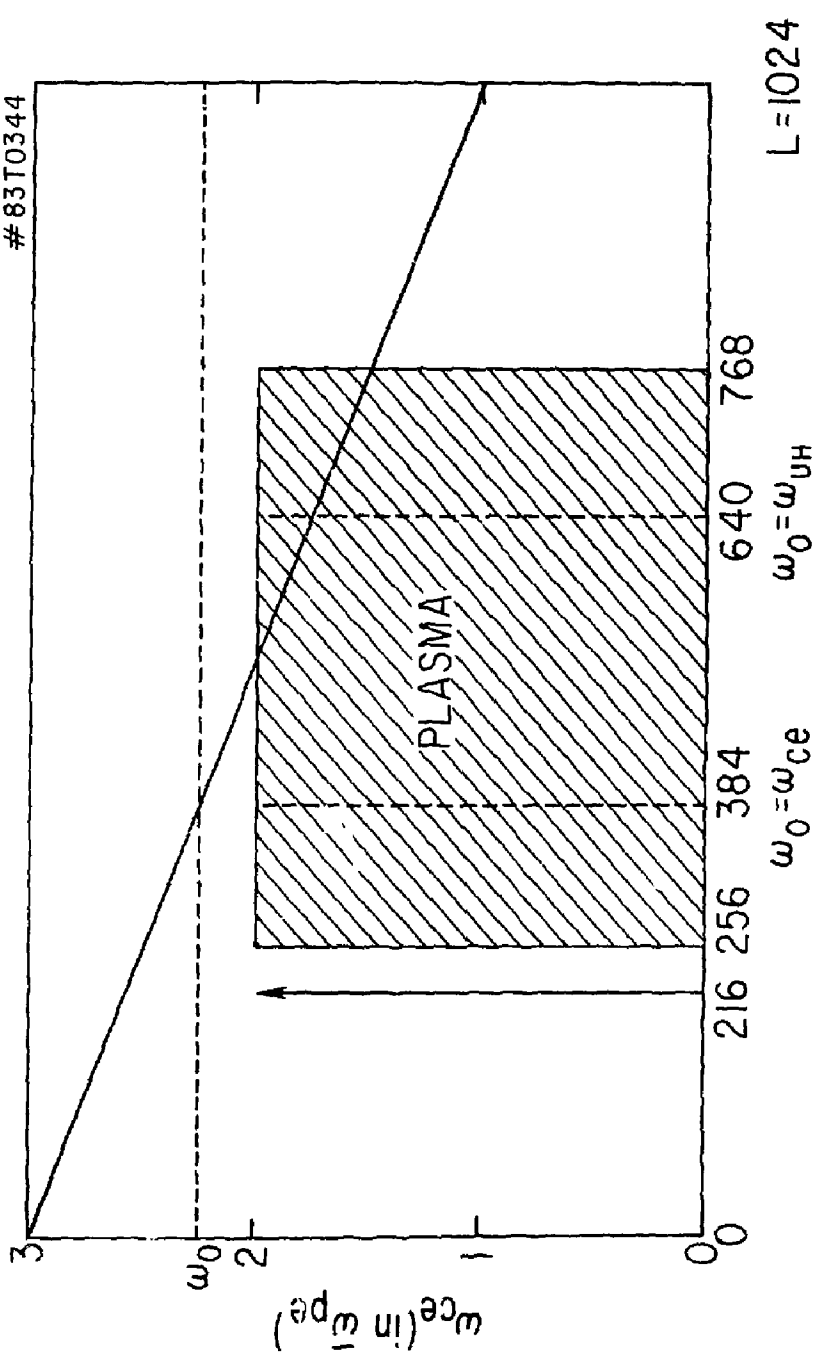
#83T0344
L=1024
PLASMA
$\omega_0=\omega_{UH}$
$\omega_0=\omega_{ce}$
ω_0
$\omega_{ce}(\text{in } \omega_{pe})$
X(in Δ)
0
216
256
384
640
768
1
2
3

Fig. 1

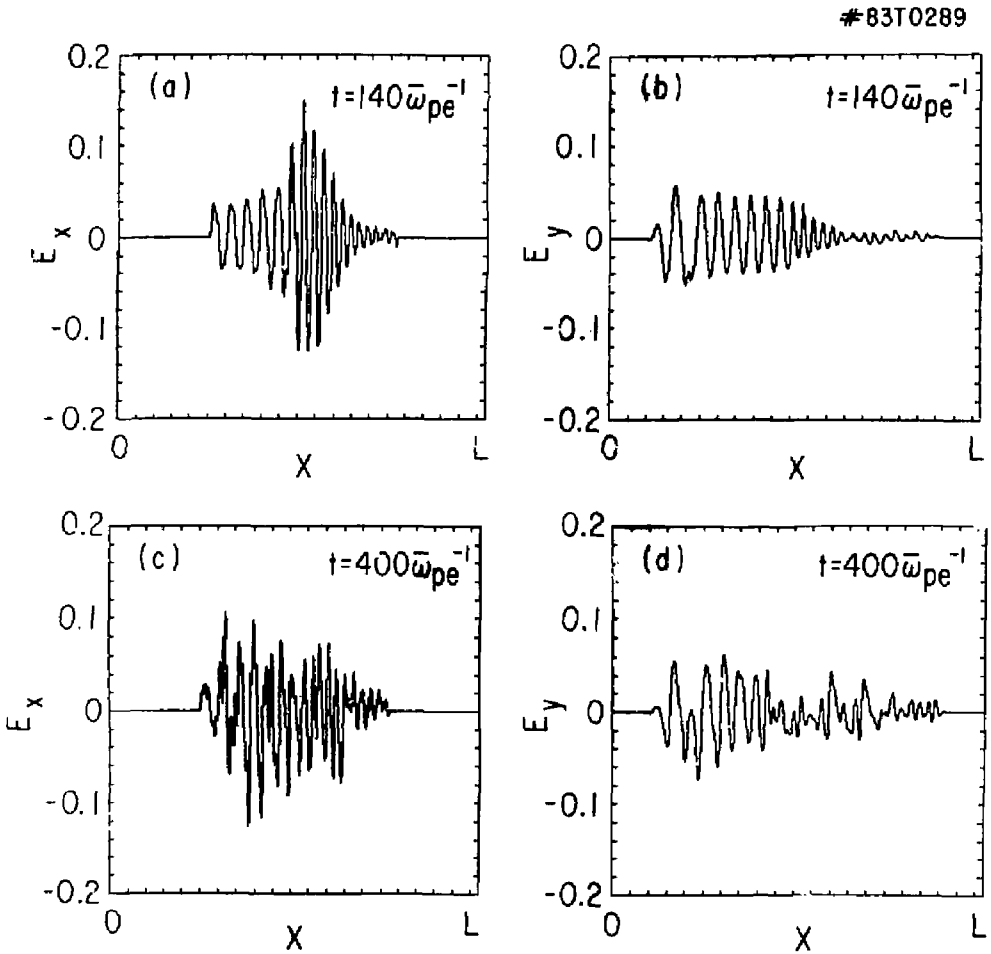
#83T0289
(a)
t=140ω̄pe⁻¹
(b)
t=140ω̄pe⁻¹
(c)
t=400ω̄pe⁻¹
(d)
t=400ω̄pe⁻¹
Ex
Ey
0.2
0.1
0
-0.1
-0.2
0
X
L

Fig. 2

#83T0290

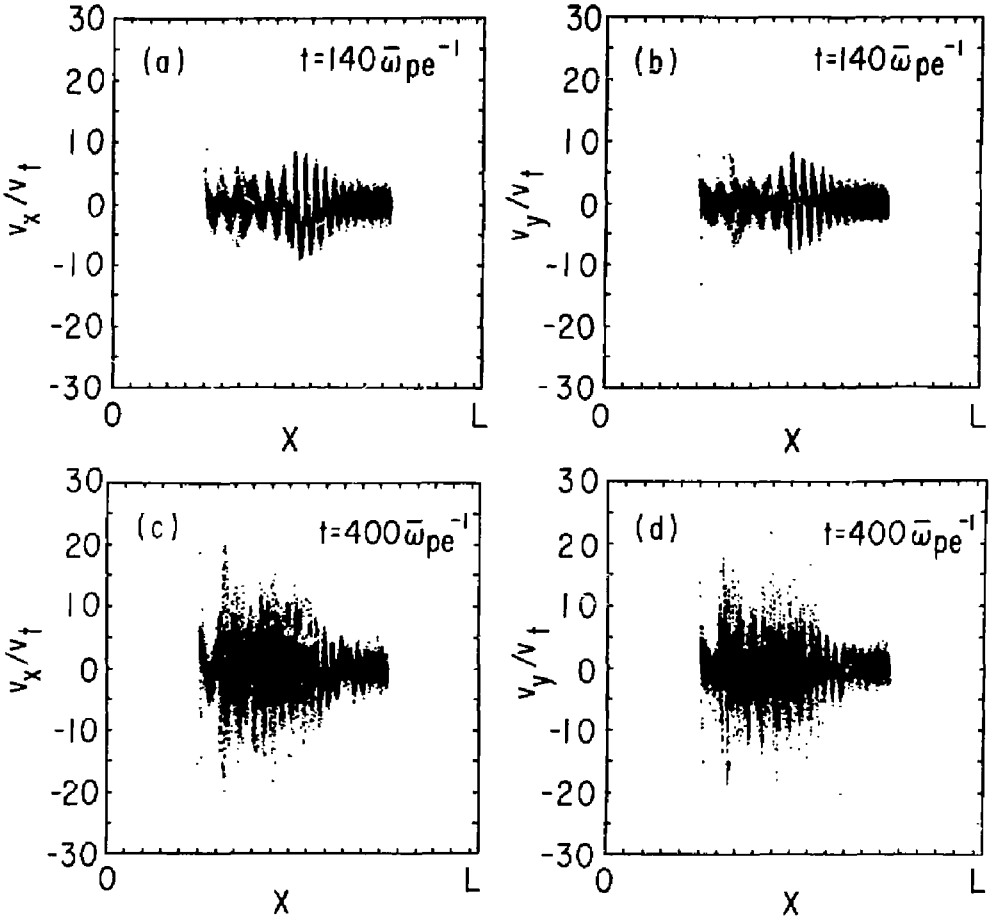

Fig. 3

83T0327

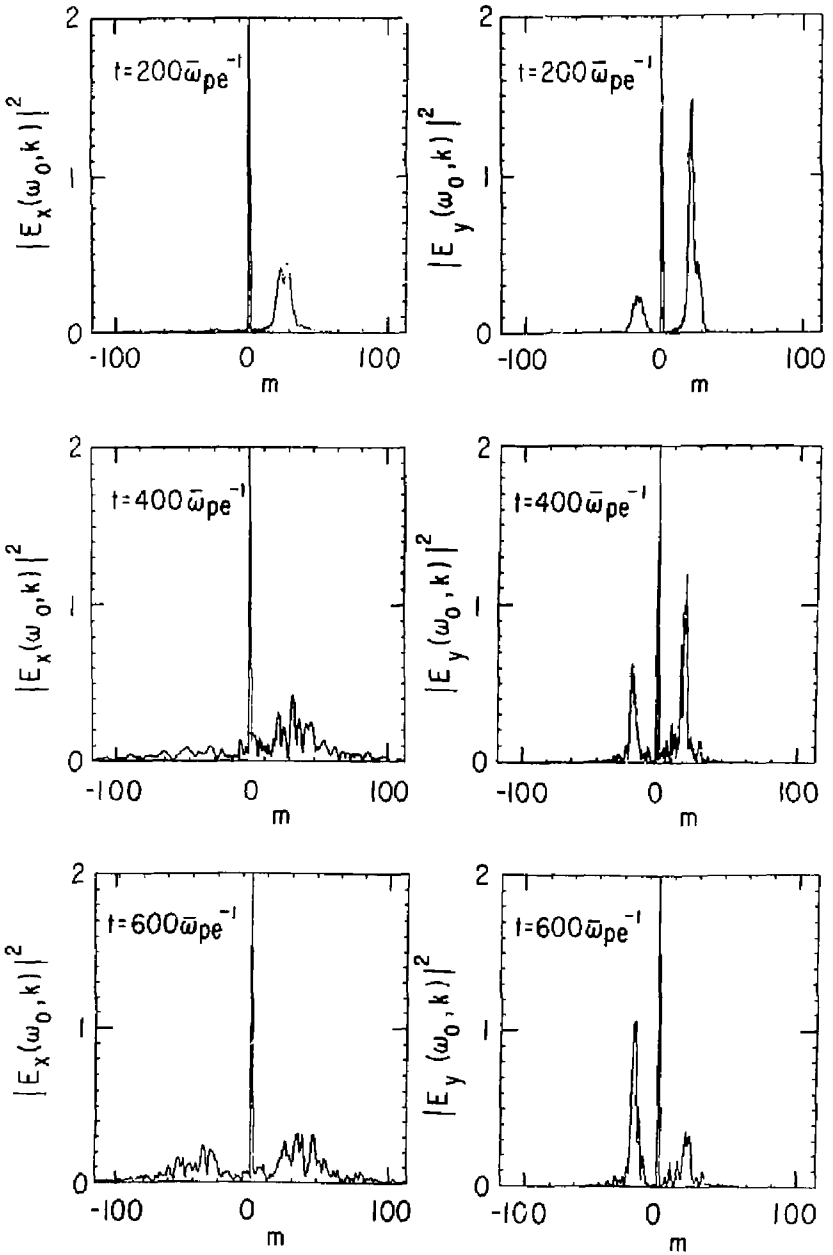

Fig. 4

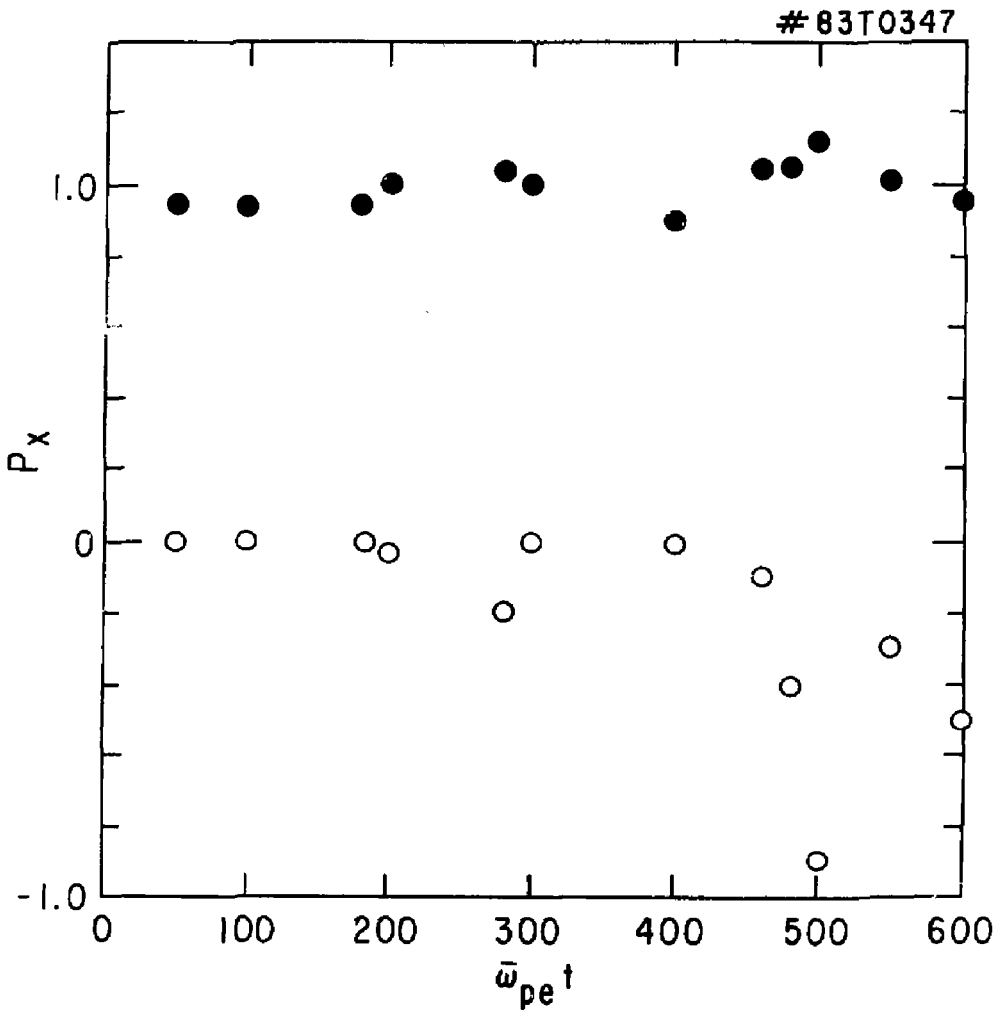

Fig. 5

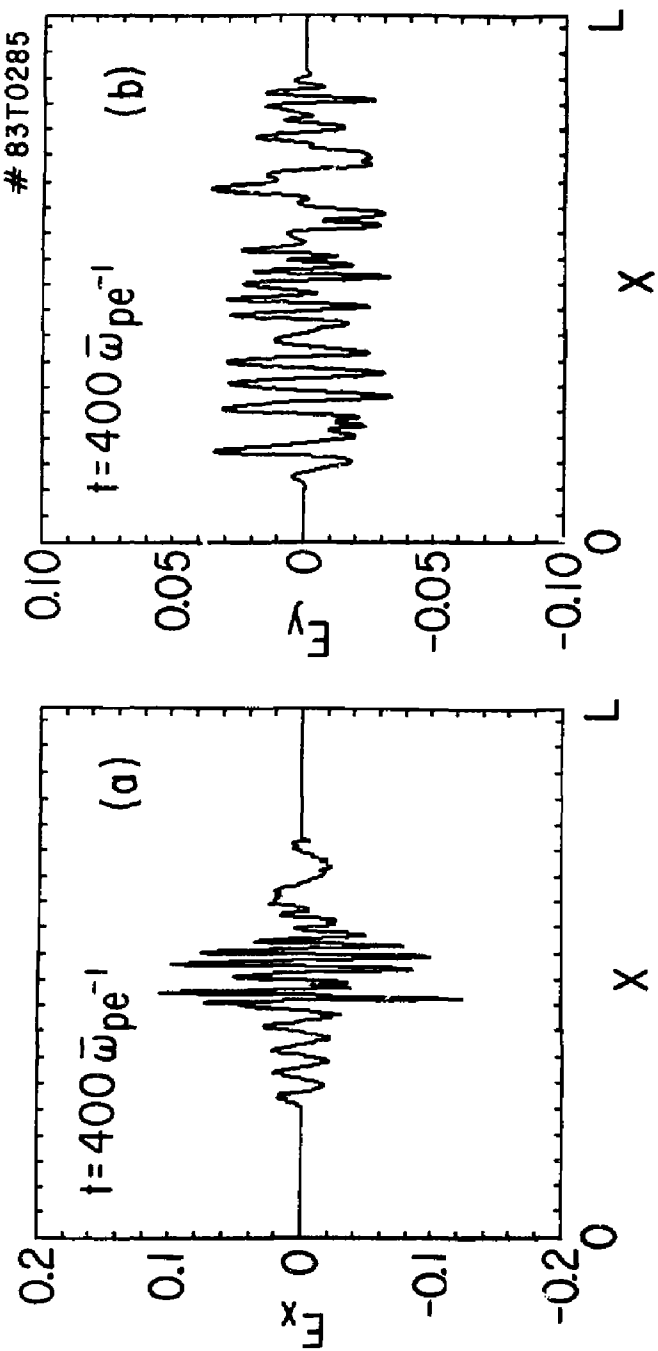
#83T0285
(a)
t=400 $\bar{\omega}_{pe}^{-1}$
E_x
0.2
0.1
0
-0.1
-0.2
0
X
L
(b)
t=400 $\bar{\omega}_{pe}^{-1}$
E_y
0.10
0.05
0
-0.05
-0.10
0
X
L

Fig. 6

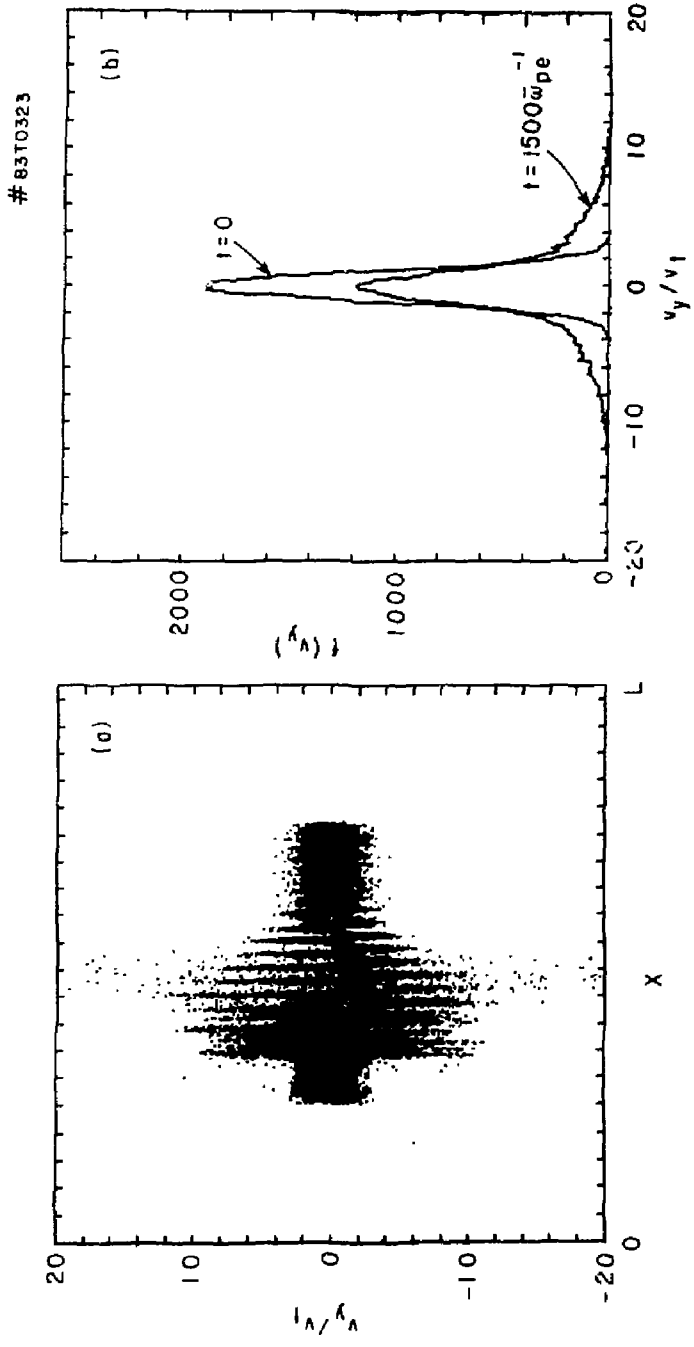

Fig. 7

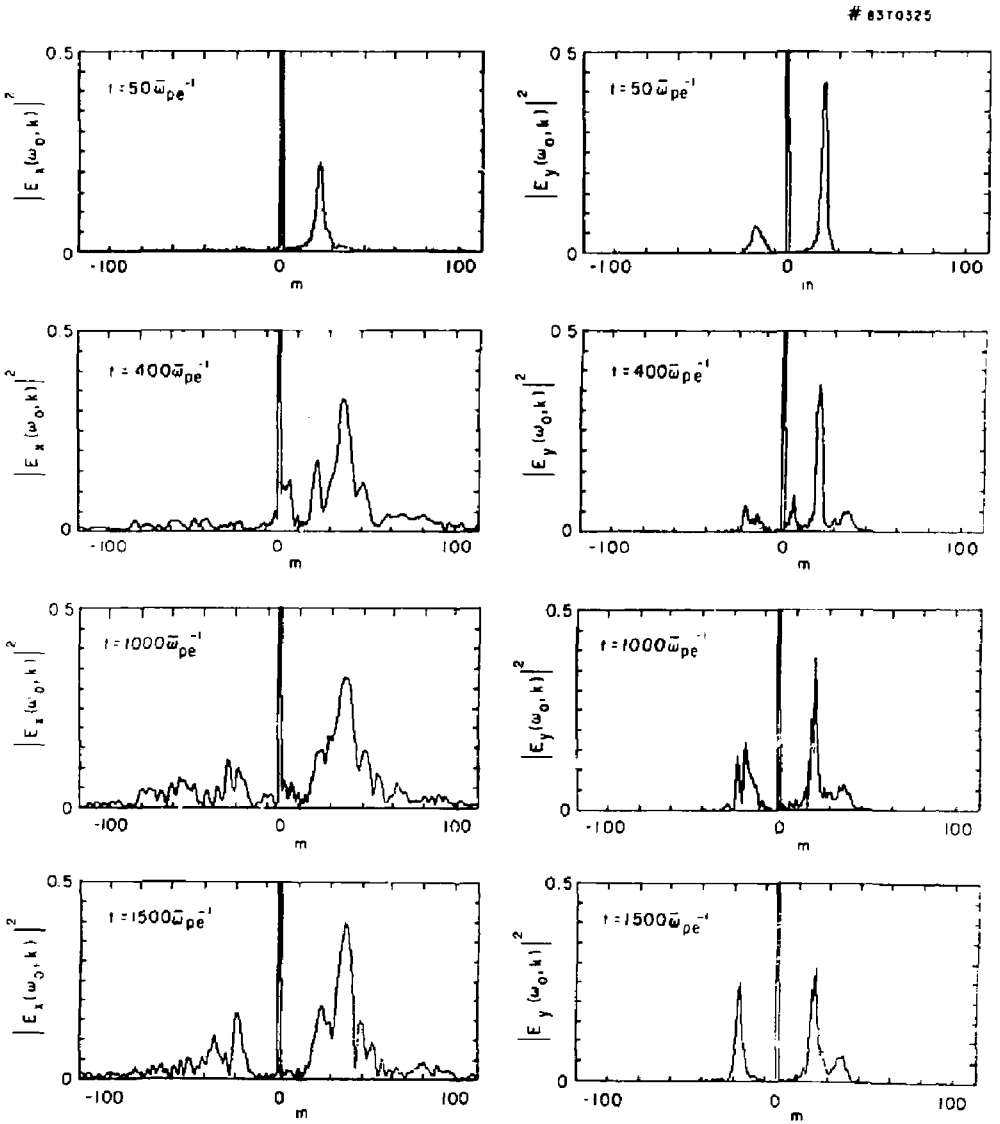
8370325
$|E_x(\omega_0,k)|^2$
$|E_y(\omega_0,k)|^2$
$t = 50\bar{\omega}_{pe}^{-1}$
$t = 400\bar{\omega}_{pe}^{-1}$
$t = 1000\bar{\omega}_{pe}^{-1}$
$t = 1500\bar{\omega}_{pe}^{-1}$
0.5
0
-100
0
100
m

Fig. 8

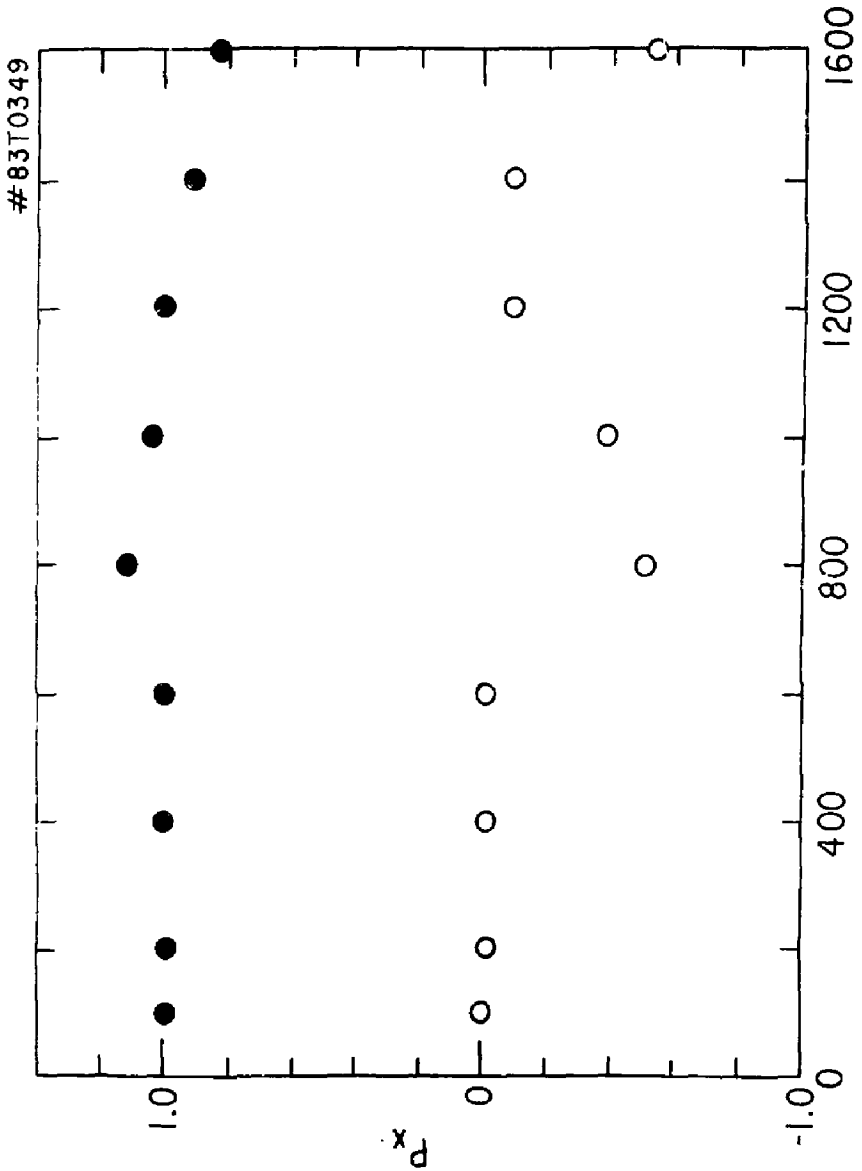

Fig. 9

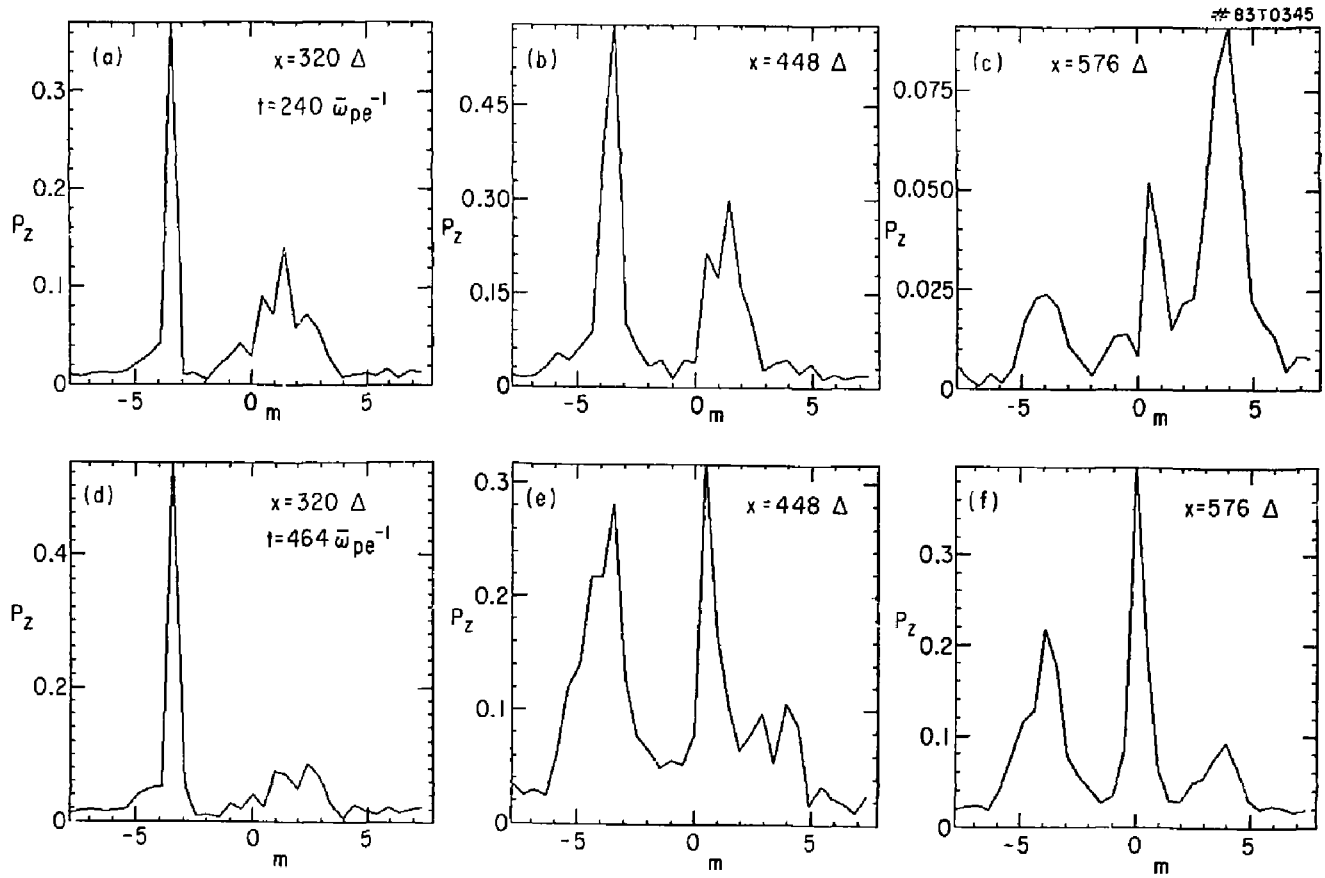
#83T0345
(a)
x=320 Δ
t=240 $\bar{\omega}_{pe}^{-1}$
(b)
x=448 Δ
(c)
x=576 Δ
(d)
x=320 Δ
t=464 $\bar{\omega}_{pe}^{-1}$
(e)
x=448 Δ
(f)
x=576 Δ
P_z
m

Fig. 10

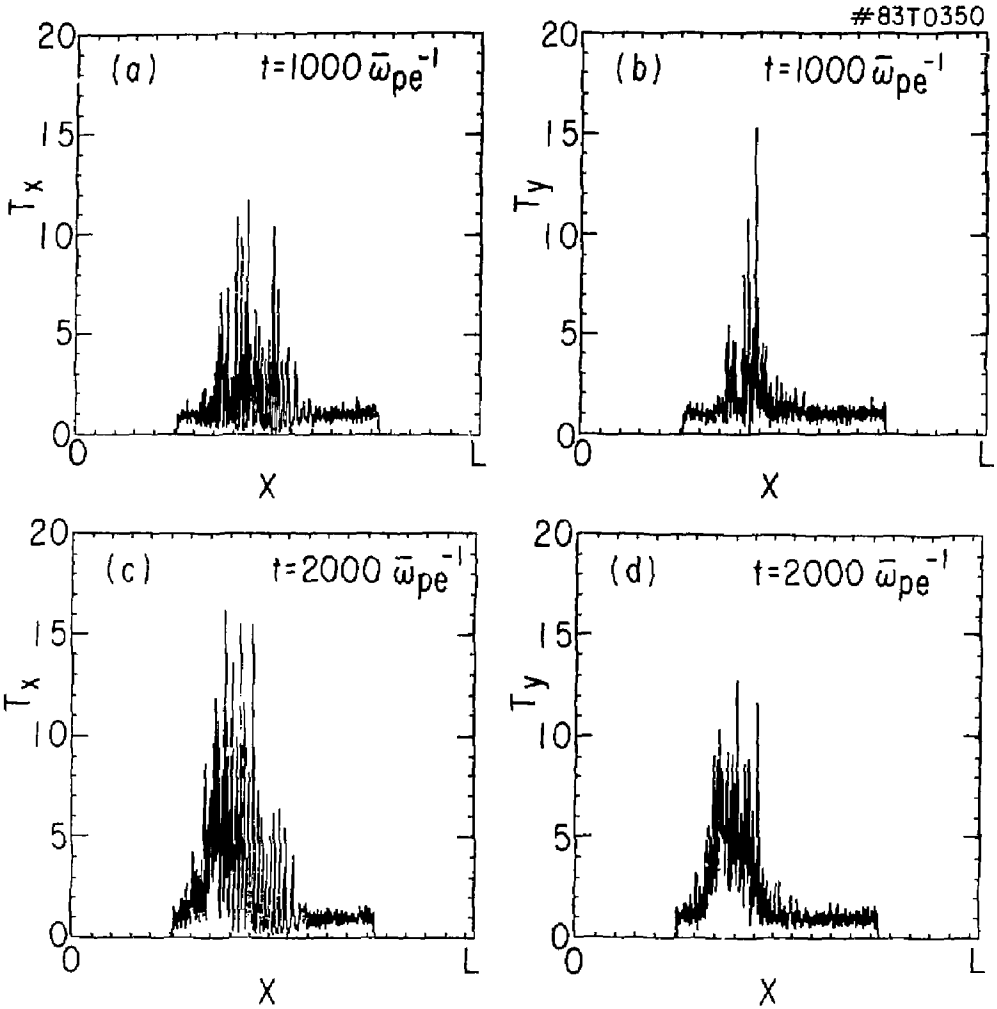
#83T0350
(a)
t=1000 $\bar{\omega}_{pe}^{-1}$
T_x
(b)
t=1000 $\bar{\omega}_{pe}^{-1}$
T_y
(c)
t=2000 $\bar{\omega}_{pe}^{-1}$
T_x
(d)
t=2000 $\bar{\omega}_{pe}^{-1}$
T_y
20
15
10
5
0
X
L

Fig. 11

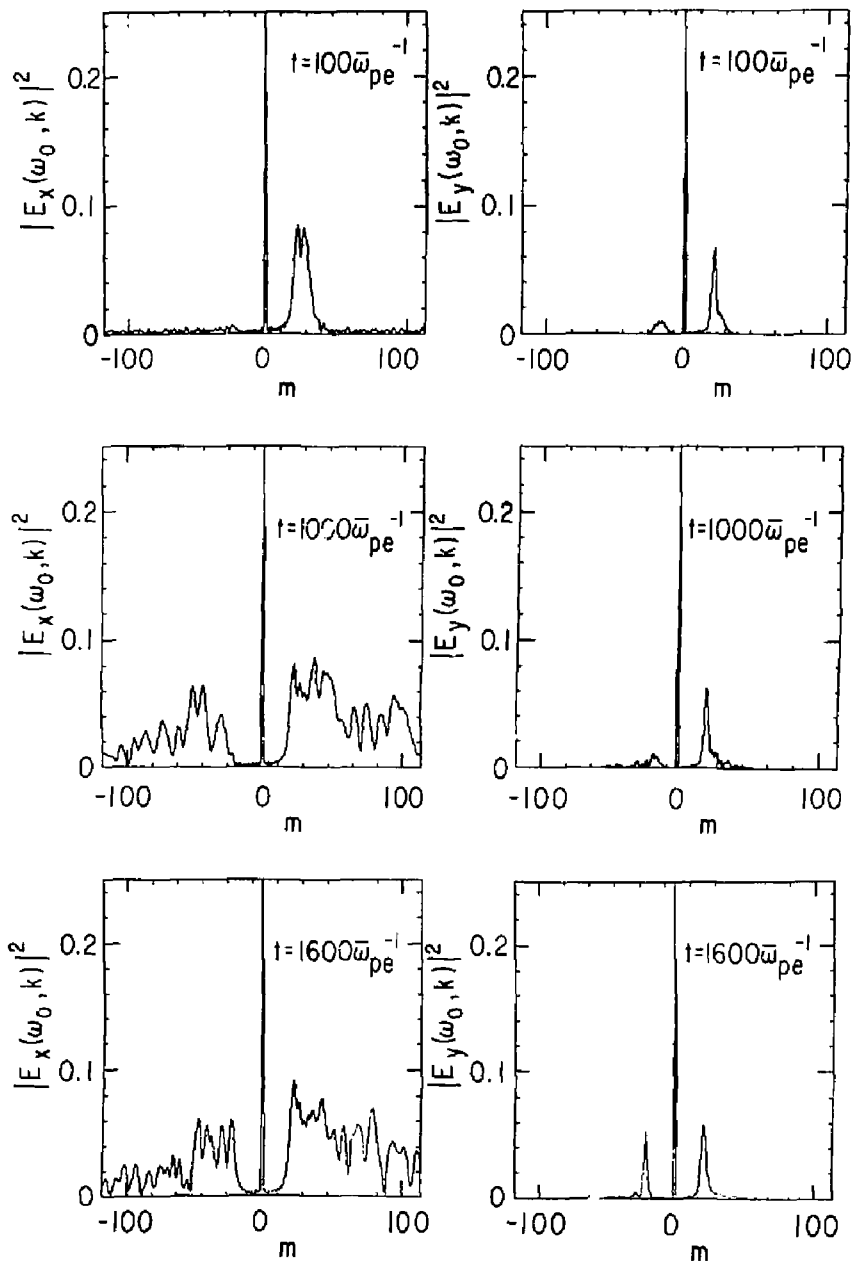
$|E_x(\omega_0,k)|^2$
$|E_y(\omega_0,k)|^2$
$t=100\bar{\omega}_{pe}^{-1}$
$t=1000\bar{\omega}_{pe}^{-1}$
$t=1600\bar{\omega}_{pe}^{-1}$
0.2
0.1
0
-100
0
100
m

Fig. 12

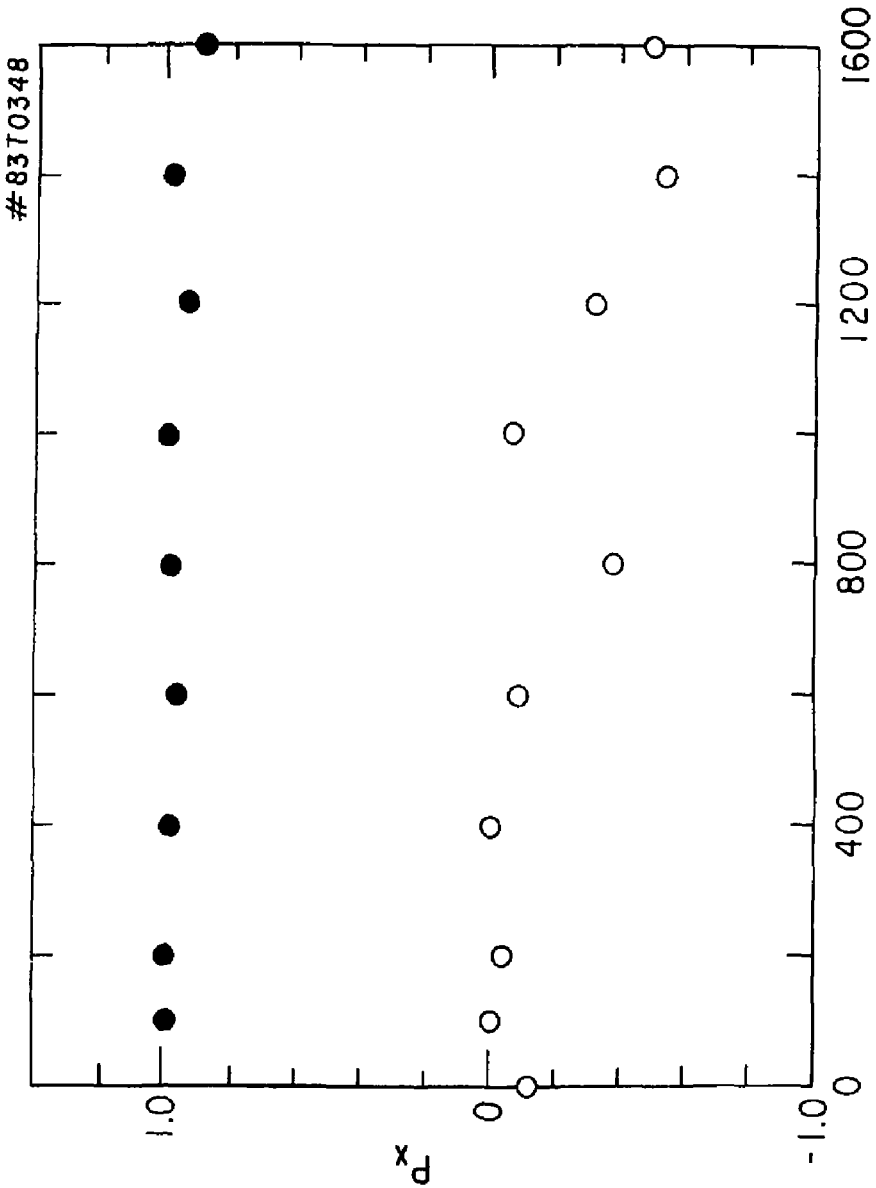

Fig. 13

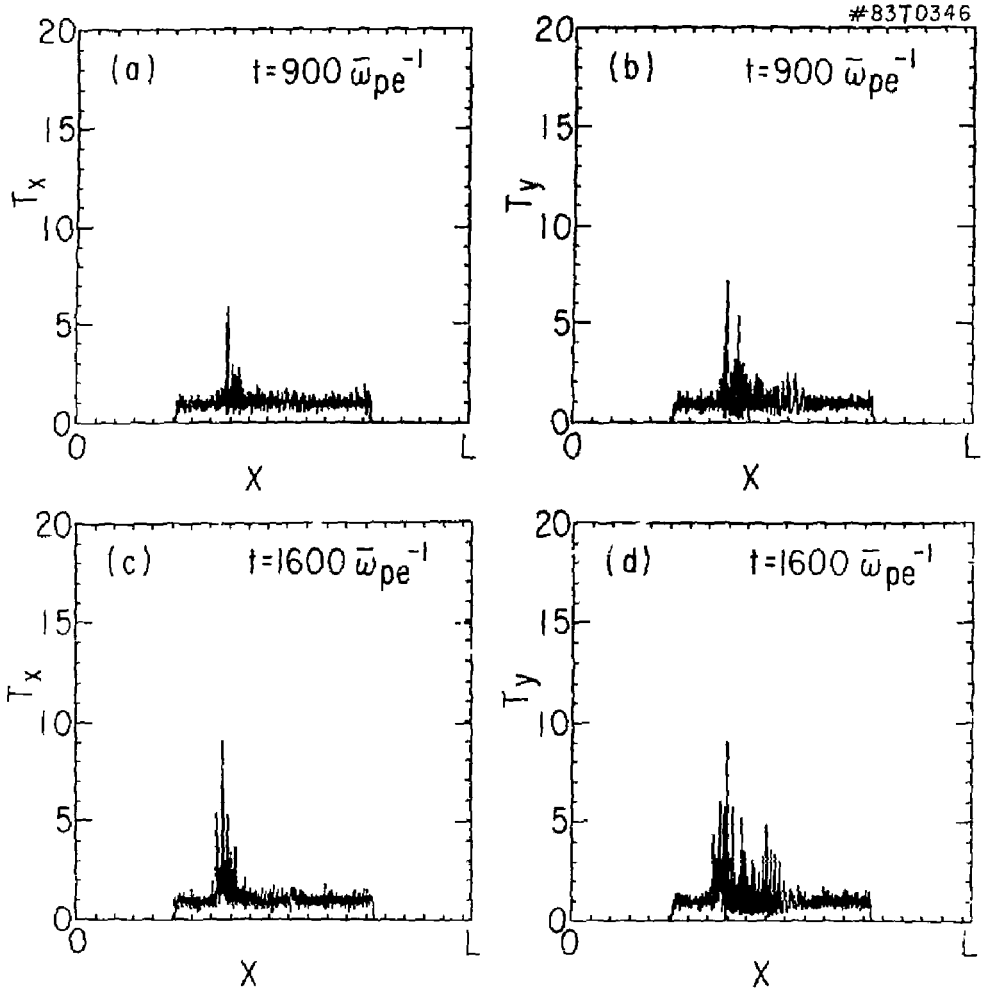
#83T0346
(a) t=900 $\bar{\omega}_{pe}^{-1}$
(b) t=900 $\bar{\omega}_{pe}^{-1}$
(c) t=1600 $\bar{\omega}_{pe}^{-1}$
(d) t=1600 $\bar{\omega}_{pe}^{-1}$
T_x
T_y
X
0
5
10
15
20
L

Fig. 14

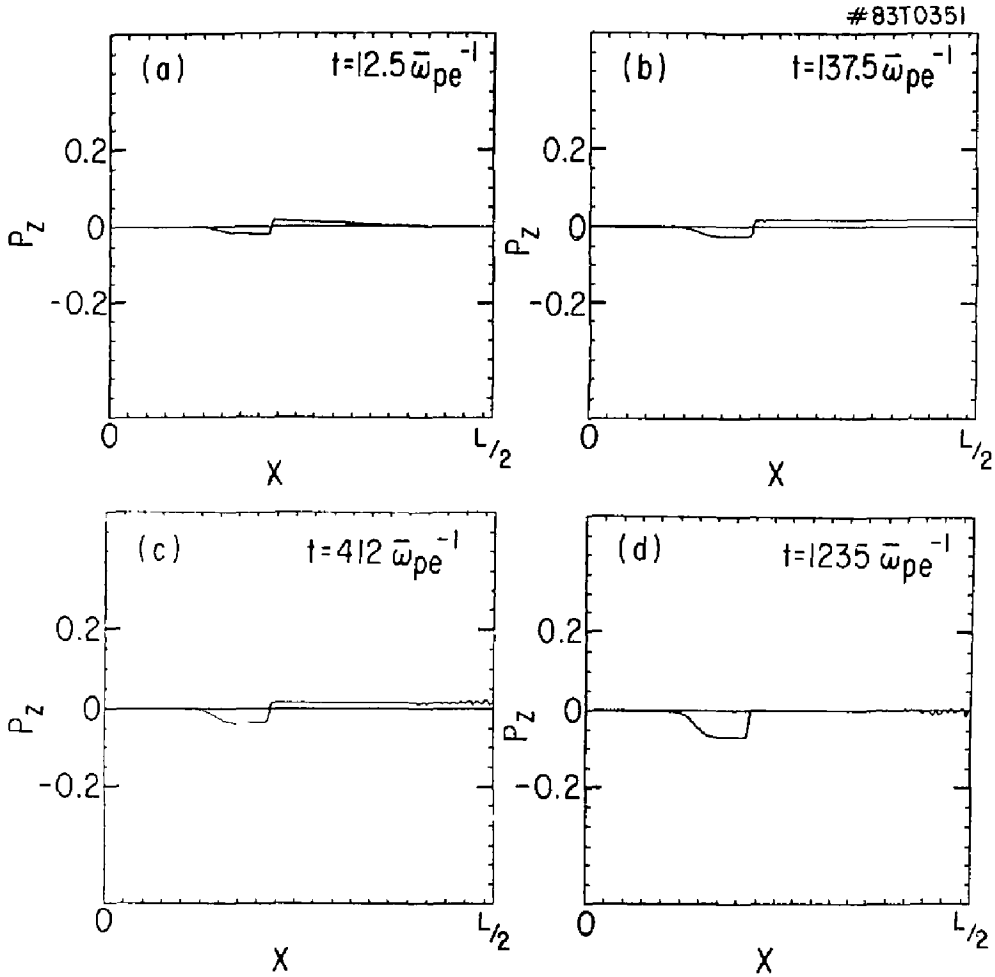
#83T0351
(a)
t=12.5 $\bar{\omega}_{pe}^{-1}$
(b)
t=137.5 $\bar{\omega}_{pe}^{-1}$
(c)
t=412 $\bar{\omega}_{pe}^{-1}$
(d)
t=1235 $\bar{\omega}_{pe}^{-1}$
P_z
0.2
0
-0.2
0
X
$L_{/2}$

Fig. 15

EXTERNAL DISTRIBUTION IN ADDITION TO TIC UC-20

Plasma Res Lab, Austra Nat'l Univ, AUSTRALIA
Dr. Frank J. Paoloni, Univ of Wollongong, AUSTRALIA
Prof. I.R. Jones, Flinders Univ., AUSTRALIA
Prof. M.H. Brennan, Univ Sydney, AUSTRALIA
Prof. F. Cap, Inst Theo Phys, AUSTRIA
Prof. Frank Verheest, Inst theoretische, BELGIUM
Dr. D. Palumbo, Dg XII Fusion Prog, BELGIUM
Ecole Royale Militaire, Lab de Phys Plasmas, BELGIUM
Dr. P.H. Sakanaka, Univ Estadual, BRAZIL
Dr. C.R. James, Univ of Alberta, CANADA
Prof. J. Teichmann, Univ of Montreal, CANADA
Dr. H.M. Skarsgard, Univ of Saskatchewan, CANADA
Prof. S.R. Sreenivasan, University of Calgary, CANADA
Prof. Tudor W. Johnston, INRS-Energie, CANADA
Dr. Hannes Barnard, Univ British Columbia, CANADA
Dr. M.P. Bachynski, MPB Technologies, Inc., CANADA
Zhengwu Li, SW Inst Physics, CHINA
Library, Tsing Hua University, CHINA
Librarian, Institute of Physics, CHINA
Inst Plasma Phys, Academia Sinica, CHINA
Dr. Peter Lukac, Komanskeho Univ, CZECHOSLOVAKIA
The Librarian, Culham Laboratory, ENGLAND
Prof. Schatzman, Observatoire de Nice, FRANCE
J. Radet, CEN-BP6, FRANCE
AM Dupas Library, AM Dupas Library, FRANCE
Dr. Tom Muel, Academy Bibliographic, HONG KONG
Preprint Library, Cent Res Inst Phys, HUNGARY
Dr. S.K. Trehan, Panjab University, INDIA
Dr. Indra, Mohan Lal Las, Banaras Hindu Univ, INDIA
Dr. L.K. Chavda, South Gujarat Univ, INDIA
Dr. R.K. Chhajlani, Var Ruchi Marg, INDIA
P. Kaw, Physical Research Lab, INDIA
Dr. Phillip Rosenau, Israel Inst Tech, ISRAEL
Prof. S. Cuperman, Tel Aviv University, ISRAEL
Prof. G. Rostagni, Univ Di Padova, ITALY
Librarian, Int'l Ctr Theo Phys, ITALY
Miss Clelia De Palo, Assoc EURATOM-CNEN, ITALY
Biblioteca, del CNR EURATOM, ITALY
Dr. H. Yamato, Toshiba Res & Dev, JAPAN
Prof. M. Yoshikawa, JAERI, Tokai Res Est, JAPAN
Prof. T. Uchida, University of Tokyo, JAPAN
Research Info Center, Nagoya University, JAPAN
Prof. Kyoji Nishikawa, Univ of Hiroshima, JAPAN
Prof. Sigeru Mori, JAERI, JAPAN
Library, Kyoto University, JAPAN
Prof. Ichiro Kawakami, Nihon Univ, JAPAN
Prof. Satoshi Itoh, Kyushu University, JAPAN
Tech Info Division, Korea Atomic Energy, KOREA
Dr. R. England, Ciudad Universitaria, MEXICO
Bibliotheek, Fom-Inst Voor Plasma, NETHERLANDS
Prof. B.S. Liley, University of Waikato, NEW ZEALAND
Dr. Suresh C. Sharma, Univ of Calabar, NIGERIA
Prof. J.A.C. Cabral, Inst Superior Tech, PORTUGAL
Dr. Octavian Petrus, ALI CUZA University, ROMANIA
Prof. M.A. Hellberg, University of Natal, SO AFRICA
Dr. Johan de Villiers, Atomic Energy Bd, SO AFRICA
Fusion Div. Library, JEN, SPAIN
Prof. Hans Wilhelmson, Chalmers Univ Tech, SWEDEN
Dr. Lennart Stenflo, University of UMEA, SWEDEN
Library, Royal Inst Tech, SWEDEN
Dr. Erik T. Karlson, Uppsala Universitet, SWEDEN
Centre de Recherchesen, Ecole Polytech Fed, SWITZERLAND
Dr. W.L. Wolse, Nat'l Bur Stand, USA
Dr. W.M. Stacey, Georg Inst Tech, USA
Dr. S.T. Wu, Univ Alabama, USA
Prof. Norman L. Oleson, Univ S Florida, USA
Dr. Benjamin Ma, Iowa State Univ, USA
Prof. Magne Kristiansen, Texas Tech Univ, USA
Dr. Raymond Askew, Auburn Univ, USA
Dr. V.T. Tolok, Kharkov Phys Tech Ins, USSR
Dr. O.D. Ryutov, Siberian Acad Sci, USSR
Dr. G.A. Eliseev, Kurchatov Institute, USSR
Dr. V.A. Glukhikh, Inst Electro-Physical, USSR
Institute Gen. Physics, USSR
Prof. T.J. Boyd, Univ College N Wales, WALES
Dr. K. Schindler, Ruhr Universitat, W. GERMANY
Nuclear Res Estab, Julich Ltd, W. GERMANY
Librarian, Max-Planck Institut, W. GERMANY
Dr. H.J. Kaeppler, University Stuttgart, W. GERMANY
Bibliothek, Inst Plasmaforschung, W. GERMANY